



# Microstructure Fingerprinting for Heterogeneously Oriented Tissue Microenvironments

Khoi Minh Huynh<sup>1,2</sup>, Ye Wu<sup>1,2</sup>, Sahar Ahmad<sup>1,2</sup>, and Pew-Thian Yap<sup>1,2</sup>(✉)

<sup>1</sup> Department of Radiology, University of North Carolina, Chapel Hill, USA

<sup>2</sup> Biomedical Research Imaging Center (BRIC), University of North Carolina,  
Chapel Hill, USA  
ptyap@med.unc.edu

**Abstract.** Most diffusion biophysical models capture basic properties of tissue microstructure, such as diffusivity and anisotropy. More realistic models that relate the diffusion-weighted signal to cell size and membrane permeability often require simplifying assumptions such as short gradient pulse and Gaussian phase distribution, leading to tissue features that are not necessarily quantitative. Here, we propose a method to quantify tissue microstructure without jeopardizing accuracy owing to unrealistic assumptions. Our method utilizes realistic signals simulated from the geometries of cellular microenvironments as fingerprints, which are then employed in a spherical mean estimation framework to disentangle the effects of orientation dispersion from microscopic tissue properties. We demonstrate the efficacy of microstructure fingerprinting in estimating intra-cellular, extra-cellular, and intra-soma volume fractions as well as axon radius, soma radius, and membrane permeability.

## 1 Introduction

In diffusion MRI, biophysical models offer a non-invasive means of probing the tissue micro-architecture of the human brain. Most models rely on closed-form formulas derived with simplifying assumptions such as short gradient pulse, Gaussian phase distribution, and the absence of compartmental exchange. The reliability and interpretability of these models diminish with deviation from these assumptions.

Monte Carlo (MC) simulations [1,2] and solving the Bloch-Torrey partial differential equation (BT-PDE) [3,4] are common methods for generating realistic signals associated with different gradient profiles and cellular geometries. However, the applications of these simulation techniques have been mostly limited to the validation of diffusion models rather than the estimation of microstructural properties.

---

This work was supported in part by the United States National Institutes of Health (NIH) through grants MH125479 and EB008374.

© The Author(s), under exclusive license to Springer Nature Switzerland AG 2023  
H. Greenspan et al. (Eds.): MICCAI 2023, LNCS 14227, pp. 131–141, 2023.  
[https://doi.org/10.1007/978-3-031-43993-3\\_13](https://doi.org/10.1007/978-3-031-43993-3_13)

Microstructure fingerprinting (MF) [5,6] exploits the representation accuracy and physical interpretability of simulated models to quantify microstructural properties. Diffusion signals are first simulated for a large collection of microstructural geometries, giving “fingerprints” of, for example, axons, somas, and the extra-cellular matrix. Tissue properties are inferred based on the relative contribution of each fingerprint to the voxel signal.

In this paper, we introduce a novel MF technique with the following key features:

1. MC simulation [5,6] is computationally expensive [1], limiting its ability in constructing a sufficient large dictionary of fingerprints for accurate tissue quantification. We will use SpinDoctor [3] to simulate diffusion signal by solving the BT-PDE. The significant speed-up of SpinDoctor over MC simulations allows fast construction of a comprehensive dictionary of fingerprints.
2. Inspired by [7], we will include fingerprints associated with different levels of membrane permeability to account for inter-cellular exchange. The utilization of simulated models has been shown to remove estimation bias associated with short exchange times [7] and to yield marked improvement and higher reproducibility over the widely used Kärger model [6].
3. Spherical Mean Spectrum Imaging (SMSI) [8] is used to eliminate confounding factors such as extra-axonal water and axonal orientation dispersion to improve sensitivity of the diffusion-weighted signal to axon radii [9].
4. MR-derived statistics are often biased toward large axons due to their dominant signal [10]. We introduce a method to correct for this bias based on signal fingerprints, offering radius and permeability measurements that are more biologically realistic.

Our method is able to efficiently and accurately probe microstructural properties such as cell size and membrane permeability without relying on assumptions associated with closed-form formulas.

## 2 Methods

### 2.1 Fingerprint Dictionary

The diffusion MRI signal at each voxel  $S$  is a combination of signals from multiple micro-environments, each represented by a signal fingerprint  $S_i$ :

$$S = \sum_i f[i] S_i(\mathcal{J}_i, \mathcal{P}), \quad (1)$$

where  $f[i]$  is the volume fraction of the  $i$ -th fingerprint,  $\mathcal{J}_i$  is a set of parameters characterizing the geometry of the corresponding micro-environment, and  $\mathcal{P}$  is a set of acquisition parameters (e.g., pulse sequence, pulse duration, etc.). For brevity, we omit  $\mathcal{P}$  as it is the same for all  $i$ 's. In [8,11],  $\mathcal{J}_i$  is based on a tensor model defined by longitudinal diffusivity  $\lambda_{\parallel}[i]$  and radial diffusivity  $\lambda_{\perp}[i]$ , yielding only basic tissue properties such as diffusivity or anisotropy. Inferring

geometrical properties such as the radius from diffusivity is not straight-forward [6]. To effectively quantify cell size and membrane permeability, we use SpinDoctor [3, 4] to generate realistic signal fingerprints for various microstructural geometries (called ‘atoms’) representing axons and somas with a range of radii and different levels of permeability in an extra-cellular matrix. Specifically, the dictionary of fingerprints covers four diffusion patterns:

1. Intra-axonal diffusion represented by packed cylinders with radii  $r \in \{0.5, 2, 2.5, 3.0, 3.5, 4.0\} \mu\text{m}$  and permeabilities  $\kappa$ ’s from 0 (impermeable) to  $50 \times 10^{-6} \mu\text{m} \mu\text{s}^{-1}$ . For  $b \leq 3000 \text{s mm}^{-2}$  (typical in most datasets), the diffusion signals of axons with radius from 0 to  $2 \mu\text{m}$  are numerically indistinguishable. The atom for  $r = 0.5 \mu\text{m}$  summarizes the distribution in  $r \in [0, 2] \mu\text{m}$  and the atoms for  $r \in [2, 4] \mu\text{m}$  capture the tail of the distribution as in [12]. Cylinders are placed in an extra-cellular space to mimic realistic configurations.
2. Extra-axonal diffusion represented using a tensor model with  $\frac{\lambda_{\parallel}}{\lambda_{\perp}} < \tau^2$ , with geometric tortuosity  $\tau = 2.6$ . We choose  $1.5 \times 10^{-3} \text{mm}^2 \text{s}^{-1} \leq \lambda_{\parallel} \leq 2.0 \times 10^{-3} \text{mm}^2 \text{s}^{-1}$ .
3. Intra-soma diffusion represented using impermeable spheres with radii from 0 to  $20 \mu\text{m}$ .
4. Free-water diffusion represented using a tensor model with  $\lambda_{\parallel} = \lambda_{\perp} > \lambda_{\text{soma-max}}$ , with  $\lambda_{\text{soma-max}} = 1.0 \times 10^{-3} \text{mm}^2 \text{s}^{-1}$  is the maximum apparent intra-soma diffusivity.

Parameters are chosen according to previous studies, covering the spectrum of biologically possible values in the human brain [6, 8, 13–20].

## 2.2 Solving the Bloch-Torrey Partial Differential Equation (BT-PDE)

We employ SpinDoctor [3] to numerically simulate the diffusion signal from a known geometry (Fig. 1) via solving the BT-PDE. SpinDoctor is typically 50 times faster than MC simulations and does not require GPUs. Our parallelized implementation generates a dictionary of fingerprints for Human Connectome Project (HCP) data with 48 intra-axonal fingerprints (6 radii and 8 permeabilities) and 20 intra-soma (20 radii) in 5 min. Note that the dictionary was generated once for the study, stored, and then resampled to match each subjects’ gradient table as in [21].

## 2.3 Solving for Volume Fractions

From [8, 11], the normalized spherical mean signal at each voxel  $\bar{E}$  is a linear combination of the normalized spherical mean signals  $\bar{E}_i$  from multiple atoms:

$$\bar{E} = \sum_i \nu[i] \bar{E}_i = \mathcal{A}\nu, \quad (2)$$

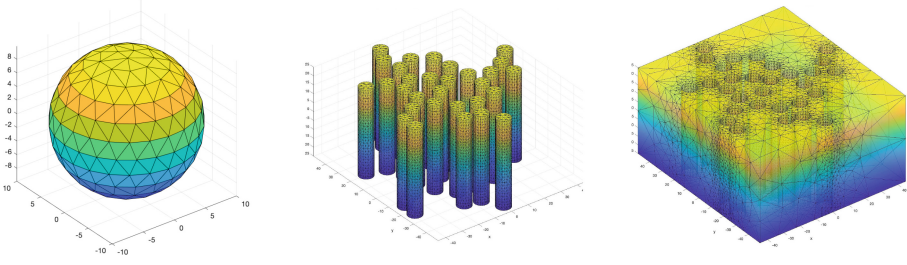


**Fig. 1. Examples of SpinDoctor Geometric Configurations.** From left to right: a sphere representing a soma with impermeable membrane, cylinders representing packed axons in a voxel, and extra-cellular space around axons allowing for compartmental exchange in case of non-zero axon permeability.

where  $\mathcal{A}$  is a matrix containing  $\bar{E}_i$  and  $\nu$  is a vector consisting of  $\nu[i]$ . Note that  $\bar{E}_i$  is a function of  $\mathcal{J}_i$  but not the direction [22]. The direction-dependent signal  $S$  can be represented using rotational spherical harmonics (SHs)  $\mathcal{R}(\mathcal{J}_i)$ , the SHs  $\mathcal{Y}_L$  of even orders up to  $L$ , and the SH coefficients  $\varphi_i$  of the fODF corresponding to the  $i$ -th fingerprint:

$$S \approx \sum_i \mathcal{R}(\mathcal{J}_i) \mathcal{Y}_L \varphi_i = \mathcal{B} \Phi. \quad (3)$$

From  $\Phi$ , the volume fraction  $\nu[i]$  of atom  $i$  is the 0-th order SH coefficient in  $\varphi_i$  [18, 23].

Following [8], to remove fiber dispersion and degeneracy confounding effect, we solve for  $\nu[i]$  by using both the spherical mean and the full signal:

1. Solve the full signal (FS) problem:

$$\min_{\Phi} \left\| \begin{pmatrix} \mathcal{B} \\ \sqrt{\gamma_1} I \end{pmatrix} \Phi - \begin{pmatrix} S \\ 0 \end{pmatrix} \right\|_2^2, \quad (4)$$

and estimate the FS problem volume fraction  $\nu_{\text{FS}}$  from  $\Phi$ .

2. Solve the mean signal (MS) problem:

$$\nu_{\text{MS}} = \arg \min_{\nu \succeq 0} \left\| \begin{pmatrix} \mathcal{A} \\ \sqrt{\gamma_2} I \end{pmatrix} \nu - \begin{pmatrix} \bar{E} \\ 0 \end{pmatrix} \right\|_2^2 + \gamma_3 \|\nu\|_1. \quad (5)$$

3. Iterative reweighing until convergence:

$$\nu_j = \arg \min_{\nu_j \succeq 0} \left\| \begin{pmatrix} \mathcal{A} \\ \sqrt{\gamma_2} I \end{pmatrix} \nu_j - \begin{pmatrix} \bar{E} \\ 0 \end{pmatrix} \right\|_2^2 + \gamma_3 \|\text{diag}(w_j) \nu_j\|_1, \quad (6)$$

where  $w_j[i] = \frac{1}{\xi + \nu_{j-1}[i]}$  with  $\xi$  being a constant and  $\nu_0$  the geometric mean of  $\nu_{\text{FS}}$  and  $\nu_{\text{MS}}$ .

We select the regularization parameters  $\gamma$ 's using the Akaike information criterion (AIC) to balance the goodness of fit and complexity of the model. There is an empirical lower bound on the soma radius that can be detected via a mixture of somas (isotropic) and axons (anisotropic) when using the mean signal alone [24]. By using the full gradient-sensitized signal in Step 1, our method can distinguish between soma (isotropic signal) and axon (anisotropic signal). Our approach with both FS and MS allows for modeling a spectrum of diffusion from fine to coarse scales without fixing the number of compartments, e.g., one in [22], two (intra-cellular and extra-cellular) in [25], or three (intra-cellular, extra-cellular, and free-water) in [26].

## 2.4 Radius Bias Correction

The average axon radius for each voxel can be calculated by averaging the radii of the respective fingerprints, weighted by the volume fractions. Since the volume fractions  $\nu$  are estimated from the normalized signal model [26], they are actually 'signal fractions'. Weighted averaging using signal fractions yields the axon radius index [17]. Since each axon's contribution to the voxel signal is approximately proportional to the square of its radius [27], using the signal fraction will create a bias toward axons with large radius [10]. This explains why the radius index is often in the range of 3 to 6  $\mu\text{m}$  [13, 17] while most axons have actual radii of 0.05 to 1.5  $\mu\text{m}$  [12, 28]. We correct for this bias by examining the microstructure model and the actual signal. The spherical mean signal  $\bar{S}(b)$  for diffusion weighting  $b$  is

$$\frac{\bar{S}(b)}{\bar{S}(0)} = \sum_i \nu[i] \frac{\bar{S}_i(b)}{\bar{S}_i(0)}, \quad (7)$$

where  $\nu[i]$  is the signal fraction and  $\bar{S}_i(b)$  is the spherical mean signal of the  $i$ -th atom. The unbiased volume fraction  $f[i]$  is given by

$$\bar{S}(b) = \sum_i f[i] \bar{S}_i(b). \quad (8)$$

Hence

$$\frac{\bar{S}(b)}{\bar{S}(0)} = \frac{1}{\bar{S}(0)} \sum_i f[i] \bar{S}_i(b) = \sum_i \nu[i] \frac{\bar{S}_i(b)}{\bar{S}_i(0)}, \quad (9)$$

allowing us to derive  $f[i]$  from  $\nu[i]$ :

$$f[i] = \nu[i] \frac{\bar{S}(0)}{\bar{S}_i(0)}. \quad (10)$$

Computing  $f$  requires the non-diffusion-weighted signal of each compartment  $\bar{S}_i(0)$ . In our case,  $\bar{S}_i(0)$ , scaled by an arbitrary factor, is known from the Spin-Doctor simulation. We define weight

$$w[i] = \frac{f[i]}{\sum_i f[i]} = \frac{\frac{\nu[i]}{\bar{S}_i(0)}}{\sum_i \frac{\nu[i]}{\bar{S}_i(0)}}, \quad (11)$$

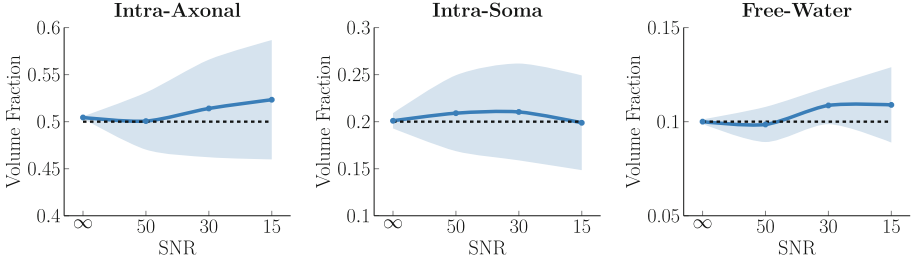


**Fig. 2. Volume Fraction.** Estimation of the volume fractions of various tissue compartments. The dashed lines represent the ground-truth values. The solid lines indicate mean values of 1000 instances at each noise level. The shaded regions indicate standard deviations.

which is not affected by the scaling factor and therefore can be used to compute the unbiased weighted-average radius.

### 3 Experiments

We validate our technique, called microstructure fingerprinting SMSI (MF-SMSI), using both in-silico and in-vivo data. The dictionary and synthetic data were generated with HCP-like parameters: 3  $b$ -shells of 1000, 2000, 3000 s mm<sup>-2</sup>, 90 directions per shell, diffusion time  $\Delta = 43.1$  ms, and pulse width  $\delta = 10.6$  ms [29].

#### 3.1 Volume Fraction

We evaluate the accuracy of MF-SMSI in volume fraction estimation by generating synthetic data following the model in [8, 26]:

$$S = \nu_{\text{FW}} S_{\text{FW}} + \nu_{\text{IS}} S_{\text{IS}} + (1 - \nu_{\text{FW}} - \nu_{\text{IS}})(\nu_{\text{IA}} S_{\text{IA}} + (1 - \nu_{\text{IA}}) S_{\text{EC}}), \quad (12)$$

where  $\nu$  and  $S$  are used to denote free-water (FW), intra-soma (IS), intra-axonal (IA), and extra-cellular (EC) volume fractions and signals. We set the ground truth volume fractions to  $\nu_{\text{FW}} = 0.1$ ,  $\nu_{\text{IS}} = 0.2$ , and  $\nu_{\text{IA}} = 0.5$ . We generated 1000 instances of the signal with SNR =  $\infty$ , 50, 30, and 15. MF-SMSI estimates accurately the volume fraction of each compartment (Fig. 2).

#### 3.2 Cell Size and Membrane Permeability

To investigate the efficacy of our bias correction, we performed three experiments:

1. Axonal radius – We simulated signals for two impermeable axons with radii 2  $\mu\text{m}$  and 4  $\mu\text{m}$ , each with volume fraction 0.5. In Fig. 3 (left panel), the axon radius is biased toward the axon with higher baseline signal, giving a large average radius, similar to the observation in [26]. Our unbiased estimate of the radius is markedly closer to the ground truth of 3  $\mu\text{m}$ .

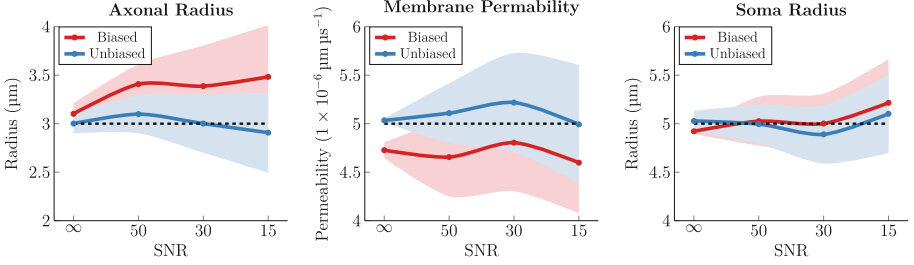


**Fig. 3. Cell Size and Membrane Permeability.** Estimation bias associated with axonal radius, membrane permeability, and soma radius. The dashed lines represent the ground truth. The solid lines indicate mean values of 1000 instances across noise levels. The shaded regions indicate standard deviations.

2. Membrane permeability – We simulated the signals for two axons with permeabilities 4 and 6 ( $\times 1 \times 10^{-6} \mu\text{m} \mu\text{s}^{-1}$ ), common radius 3  $\mu\text{m}$ , and equal volume fraction 0.5. In Fig. 3 (middle panel), the biased permeability estimate is biased toward the axon with lower permeability and therefore higher baseline signal. MF-SMSI is able to estimate the correct permeability value matching the ground truth of  $5 \times 1 \times 10^{-6} \mu\text{m} \mu\text{s}^{-1}$ .
3. Soma radius – We simulated signals for two somas with radii 4  $\mu\text{m}$  and 6  $\mu\text{m}$  with equal volume fraction 0.5. From Fig. 3 (right panel), the bias toward the soma with higher radius (higher baseline signal) is not severe. MF-SMSI yields estimate of the soma radius that is closer to the ground truth.

### 3.3 In-vivo Data

We compare our estimates with the axonal radius index  $r_{\text{axon}}^{\text{index}}$  from ActiveAx [27]. Figure 4 presents the averaged MF-SMSI and ActiveAx maps of 35 HCP subjects. Intra-axonal ( $\nu_{\text{IA}}$ ), extra-cellular ( $\nu_{\text{EC}}$ ), free-water ( $\nu_{\text{FW}}$ ), and intra-soma ( $\nu_{\text{IS}}$ ) volume fractions are in great agreement with previous studies [8, 19, 20, 25]. Briefly,  $\nu_{\text{IA}}$  is higher in white matter,  $\nu_{\text{FW}}$  is high in CSF, and  $\nu_{\text{IS}}$  is high in the cortical ribbon.

Axonal radius and permeability are lower in deep white matter, especially at the body of the corpus callosum and the forceps major, where axons are myelinated and densely packed [8]. Axonal radius  $r_{\text{axon}}$  ranges from 1.4  $\mu\text{m}$  to 1.7  $\mu\text{m}$  in most white matter areas with a small increase toward the cortex, similar to observations reported in histological studies [12, 30, 31]. Axonal radii are slightly lower in the anterior than the posterior part of the brain, in line with [6, 13]. ActiveAx  $r_{\text{axon}}^{\text{index}}$  is overestimated with values ranging from 3.5 to 7  $\mu\text{m}$  with abrupt spatial changes: almost doubled from the corpus callosum to the cortex, which is unrealistic as the spatial variation of axonal radii was reported to be small [12, 15, 32].

The soma radii  $r_{\text{soma}}$  in the cortical ribbon have a mean value of 11  $\mu\text{m}$ , similar to what was reported in [19].

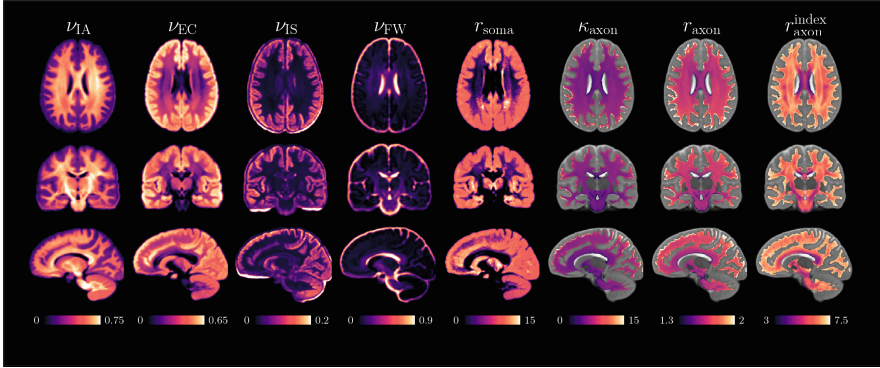


**Fig. 4. Microstructural Measurements.** Averaged microstructural indices from 35 HCP subjects. Top panel: Intra-axonal  $\nu_{IA}$ , extra-cellular  $\nu_{EC}$ , intra-soma  $\nu_{IS}$ , and free-water  $\nu_{FW}$  volume fractions. Bottom panel: soma radius  $r_{soma}$  ( $\mu\text{m}$ ), axonal permeability  $\kappa_{axon}$  ( $1 \times 10^{-6} \mu\text{m} \mu\text{s}^{-1}$ ), axonal radius  $r_{axon}$  ( $\mu\text{m}$ ), and ActiveAx axon radius index  $r_{axon}^{index}$  ( $\mu\text{m}$ ). Axonal measurements (overlaid on T2w images) are shown in white matter only.

### 3.4 Histological Corroboration

We compare our axonal radius estimate  $r_{axon}$ , ActiveAx axonal radius index  $r_{axon}^{index}$ , and the effective axon radius  $r_{eff}$  from [9], with histological samples

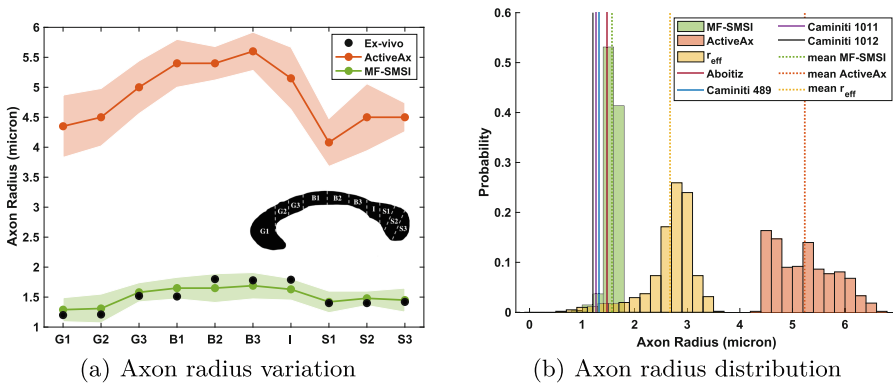


**Fig. 5. Histological Evidence.** Left: Mean axonal radii of 35 subjects in different regions of the corpus callosum given by MF-SMSI and ActiveAx. Shaded areas mark the standard deviations. Ex-vivo values are calculated from [12]. Right: Radius distribution in the corpus callosum. Histograms show the distributions and their mean values (marked with dotted lines) for MF-SMSI (unbiased estimate), ActiveAx (radius index), and effective axonal radii (Fig. 7 in [9]). The solid vertical lines show the mean values from histological studies [12, 32] (accounted for shrinkage).



reported in [12,32]. Histological values were multiplied by 1.2 to correct for ex-vivo shrinkage [9].

Figure 5(a) shows the mean axonal radii estimated with MF-SMSI and ActiveAx for different areas of the corpus callosum from HCP subjects. Overall, there is a low-high-low trend going from the genu (anterior) through the mid-body to the splenium (posterior) of the corpus callosum. Ex-vivo values (after shrinkage correction) fall almost entirely in the range calculated with MF-SMSI, indicating strong agreement between our results and histological measurements.

Figure 5(b) shows the distribution of mean axonal radius in the corpus callosum from MF-SMSI, ActiveAx, and  $r_{\text{eff}}$  from [9]. Unlike Active Ax  $r_{\text{axon}}^{\text{index}}$  and  $r_{\text{eff}}$ , which are indicators of axon radii, our estimates of  $r_{\text{axon}}$  are more realistic measurements of axonal radii, closer to ex-vivo samples.

## 4 Conclusion

We have presented a microstructure fingerprinting method that can provide accurate and reliable measurements of tissue properties beyond diffusivity and anisotropy, allowing quantification of cell size and permeability associated with axons and somas.

## References

1. Hall, M.G., Alexander, D.C.: Convergence and parameter choice for Monte-Carlo simulations of diffusion MRI. *IEEE Trans. Med. Imaging* **28**(9), 1354–1364 (2009)
2. Balls, G., Frank, L.: A simulation environment for diffusion weighted MR experiments in complex media. *Magn. Reson. Med.* **62**(3), 771–778 (2009)
3. Li, J.R., et al.: SpinDoctor: a Matlab toolbox for diffusion MRI simulation. *Neuroimage* **202**, 116120 (2019)
4. Fang, C., Nguyen, V.D., Wassermann, D., Li, J.R.: Diffusion MRI simulation of realistic neurons with SpinDoctor and the Neuron Module. *Neuroimage* **222**, 117198 (2020)
5. Rensonnet, G., et al.: Towards microstructure fingerprinting: estimation of tissue properties from a dictionary of Monte Carlo diffusion MRI simulations. *Neuroimage* **184**, 964–980 (2019)
6. Nedjati-Gilani, G.L., et al.: Machine learning based compartment models with permeability for white matter microstructure imaging. *Neuroimage* **150**, 119–135 (2017)
7. Nilsson, M., Alerstam, E., Wirestam, R., Sta, F., Brockstedt, S., Lätt, J., et al.: Evaluating the accuracy and precision of a two-compartment Kärger model using Monte Carlo simulations. *J. Magn. Reson.* **206**(1), 59–67 (2010)
8. Huynh, K.M., et al.: Probing tissue microarchitecture of the baby brain via spherical mean spectrum imaging. *IEEE Trans. Med. Imaging* **39**(11), 3607–3618 (2020)
9. Veraart, J., et al.: Noninvasive quantification of axon radii using diffusion MRI. *eLIFE* **9**, e49855 (2020)
10. Frigo, M., Fick, R., Zucchelli, M., Deslauriers-Gauthier, S., Deriche, R.: Multi tissue modelling of diffusion MRI signal reveals volume fraction bias. In: *International Symposium on Biomedical Imaging*. (2020)

11. Huynh, K.M., et al.: Probing brain micro-architecture by orientation distribution invariant identification of diffusion compartments. In: International Conference on Medical Image Computing and Computer-Assisted Intervention, Springer, pp. 547–555 (2019)
12. Aboitiz, F., Scheibel, A.B., Fisher, R.S., Zaidel, E.: Fiber composition of the human corpus callosum. *Brain Res.* **598**(1–2), 143–153 (1992)
13. Fan, Q., et al.: Axon diameter index estimation independent of fiber orientation distribution using high-gradient diffusion MRI. *NeuroImage* **222** 117197 (2020)
14. Imae, T., et al.: Estimation of cell membrane permeability and intracellular diffusion coefficient of human gray matter. *Magn. Reson. Med. Sci.* **8**(1), 1–7 (2009)
15. Veraart, J., Raven, E.P., Edwards, L.J., Weiskopf, N., Jones, D.K.: The variability of MR axon radii estimates in the human white matter. *Hum. Brain Mapp.* **42**(7), 2201–2213 (2021)
16. Walter, A., Gutknecht, J.: Permeability of small nonelectrolytes through lipid bilayer membranes. *J. Membr. Biol.* **90**(3), 207–217 (1986)
17. Zhang, H., Hubbard, P.L., Parker, G.J., Alexander, D.C.: Axon diameter mapping in the presence of orientation dispersion with diffusion MRI. *Neuroimage* **56**(3), 1301–1315 (2011)
18. White, N.S., Leergaard, T.B., D’Arceuil, H., Bjaalie, J.G., Dale, A.M.: Probing tissue microstructure with restriction spectrum imaging: histological and theoretical validation. *Hum. Brain Mapp.* **34**(2), 327–346 (2013)
19. Palombo, M., et al.: SANDI: a compartment-based model for non-invasive apparent soma and neurite imaging by diffusion MRI. *NeuroImage* **215** 116835 (2020)
20. Huynh, K.M., et al.: Characterizing intra-soma diffusion with spherical mean spectrum imaging. In: International Conference on Medical Image Computing and Computer-Assisted Intervention, Springer, pp. 354–363 (2020)
21. Daducci, A., Canales-Rodríguez, E.J., Zhang, H., Dyrby, T.B., Alexander, D.C., Thiran, J.P.: Accelerated microstructure imaging via convex optimization (AMICO) from diffusion MRI data. *Neuroimage* **105**, 32–44 (2015)
22. Kaden, E., Kruggel, F., Alexander, D.C.: Quantitative mapping of the per-axon diffusion coefficients in brain white matter. *Magn. Reson. Med.* **75**(4), 1752–1763 (2016)
23. Tournier, J.D., Calamante, F., Gadian, D.G., Connelly, A.: Direct estimation of the fiber orientation density function from diffusion-weighted MRI data using spherical deconvolution. *Neuroimage* **23**(3), 1176–1185 (2004)
24. Afzali, M., Nilsson, M., Palombo, M., Jones, D.K.: Spheriously? the challenges of estimating sphere radius non-invasively in the human brain from diffusion MRI. *Neuroimage* **237**, 118183 (2021)
25. Kaden, E., Kelm, N.D., Carson, R.P., Does, M.D., Alexander, D.C.: Multi-compartment microscopic diffusion imaging. *Neuroimage* **139**, 346–359 (2016)
26. Zhang, H., Schneider, T., Wheeler-Kingshott, C.A., Alexander, D.C.: NODDI: practical in vivo neurite orientation dispersion and density imaging of the human brain. *Neuroimage* **61**(4), 1000–1016 (2012)
27. Alexander, D.C., et al.: Orientationally invariant indices of axon diameter and density from diffusion MRI. *Neuroimage* **52**(4), 1374–1389 (2010)
28. Drobniak, I., Neher, P., Poupon, C., Sarwar, T.: Physical and digital phantoms for validating tractography and assessing artifacts. *Neuroimage* **245**, 118704 (2021)
29. Van Essen, D.C., et al.: The WU-Minn human connectome project: an overview. *Neuroimage* **80**, 62–79 (2013)

30. Liewald, D., Miller, R., Logothetis, N., Wagner, H.-J., Schüz, A.: Distribution of axon diameters in cortical white matter: an electron-microscopic study on three human brains and a macaque. *Biol. Cybern.* **108**(5), 541–557 (2014). <https://doi.org/10.1007/s00422-014-0626-2>
31. Sepehrband, F., Alexander, D.C., Kurniawan, N.D., Reutens, D.C., Yang, Z.: Towards higher sensitivity and stability of axon diameter estimation with diffusion-weighted MRI. *NMR Biomed.* **29**(3), 293–308 (2016)
32. Caminiti, R., Ghaziri, H., Galuske, R., Hof, P.R., Innocenti, G.M.: Evolution amplified processing with temporally dispersed slow neuronal connectivity in primates. *Proc. Natl. Acad. Sci.* **106**(46), 19551–19556 (2009)